Analysis of CM Volt-Second Influence on CM Inductor Saturation and Design for Input EMI Filters in Three-Phase DC-Fed Motor Drive Systems

Fang Luo, *Student Member, IEEE*, Shuo Wang, *Senior Member, IEEE*, Fei (Fred) Wang, *Fellow, IEEE*, Dushan Boroyevich, *Fellow, IEEE*, Nicolas Gazel, Yong Kang, and Andrew Carson Baisden, *Student Member, IEEE*

***Abstract*—Common-mode (CM) choke saturation is a practical problem in CM filter applications. It is generally believed that the leakage inductance of CM chokes makes the core saturated. This paper analyzes two new mechanisms for CM choke saturation due to CM voltage, and these mechanisms are verified in experiment. CM choke saturation is particularly important for motor drive systems, which have a high CM voltage and comparably higher stray grounding capacitance. A model is established to describe the relationship between the CM voltage and the volume of the CM magnetic components. According to the analysis, line impedance stabilization networks (LISNs) play an important role in the design of CM magnetic components.**

***Index Terms*—Common-mode (CM) inductor, CM voltage, volt-second.**

I. Introduction

COMMON-MODE (CM) filters play an important role for noise reduction in power-electronic systems, but the CM magnetic component can take up to 25% of the system volume. The saturation of the CM inductor core is a complex and important issue in electromagnetic interference (EMI) filter design. In previous literature [1]–[3], it has been proven that saturation can be caused by the leakage inductance. However, in practice, the CM choke can still be saturated even if it is designed with leakage inductance and differential mode (DM) current constraints. Although overdesigning the magnetic component is a safe way to prevent the core from saturation, the resulting bulky size is not desirable for high-power-density converter design. Sun and coworkers [4]–[6] determined that for three-phase ac–dc–ac motor drive systems, CM voltage can be a factor determining flux density inside CM magnetic cores. However, it is still unknown how the CM voltage impacts the CM choke flux density and how to use this information in design.

There are lots of works have been done on the analysis of CM noise propagation path. Ran *et al*. [16], Akagi and Oe [17], Akagi and Shimizu [18], and Baiju *et al*. [19] determined that neutral-point voltage/CM voltage in three-phase motor drive systems has a significant impact on the CM EMI noise level. Motor drive systems mentioned in those papers are ac–dc–ac systems. The CM filtering capacitors on input ac side, and heat-sink stray capacitance, along with the stray grounding capacitance inside the motor create the low-impedance CM noise path. The neutral CM voltage can be considered as the noise source. The CM voltage is calculated in [16]–[19] to estimate the CM leakage current. However, these analyses focus on ac–dc–ac systems not specifically for dc-fed motor drives. In these papers, several kinds of line EMI filters are designed. However, how the CM volt-second impacts the magnetic component design and how it impacts the saturation and magnetic volume is not clearly addressed. In most of references, CM choke design still follows the constraint: saturation flux density is determined by leakage inductance and DM current [12].

This paper focuses on a new mechanism of CM choke saturation caused by CM voltage. It contains two aspects that are related to the CM voltage and CM volt-second: CM noise path resonance and converter operating point. This paper proved that the CM voltage/CM volt-second can actually determine the CM flux density of CM choke, and cause the CM chokes to saturate. Hence, the CM voltage can directly determine the volume of CM magnetic component, and the CM choke volume can be evaluated by calculating CM voltage. This relationship can be used as a design criterion for CM core selection in high density EMI filter design.

A dc-fed three-phase motor drive system usually has a high line-to-ground impedance, but in EMI test when line impedance stabilization networks (LISNs) are installed, they can create a low-grounding-impedance path, which increases CM volt-second and makes the CM chokes bigger. In this paper, analyses have been done to uncover how the LISNs impact the CM noise path, and how the LISNs impact CM voltage on the CM choke.

Manuscript received September 25, 2009; revised December 24, 2009. Date of current version June 18, 2010. This work was supported by the SAFRAN Group. The work of F. Luo was supported by the Chinese Scholarship Council and Huazhong University of Science and Technology. Recommended for publication by Associate Editor J.-L. Schanen.

F. Luo and D. Boroyevich are with the Department of Electrical and Computer Engineering, Center for Power Electronics Systems (CPES), Virginia Polytechnic Institute and State University (Virginia Tech), Blacksburg, VA 24060 USA (e-mail: fangluo@vt.edu; dushan@vt.edu).

S. Wang is with the Electrical Power Systems, GE Aviation Systems, Vandalia, OH 45377 USA (e-mail: shwang6@vt.edu).

F. (Fred) Wang is with the University of Tennessee, Knoxville, TN 37916 USA (e-mail: fred.wang@utk.edu).

N. Gazel is with the Safran Group, Safran Power, Hispano-Suiza, Moissy Cramayel 77551, France (e-mail: nicolas.gazel@hispano-suiza-sa.com).

Y. Kang is with the Department of Electrical and Electronic Engineering, Huazhong University of Science and Technology, Wuhan 430074, China (e-mail: ykang@mail.hust.edu.cn).

A. C. Baisden is with the Johns Hopkins University Applied Physics Laboratory, Laurel, MD 20723 USA (e-mail: cbaisden@vt.edu).

Color versions of one or more of the figures in this paper are available online at http://ieeexplore.ieee.org.

Digital Object Identifier 10.1109/TPEL.2010.2043541

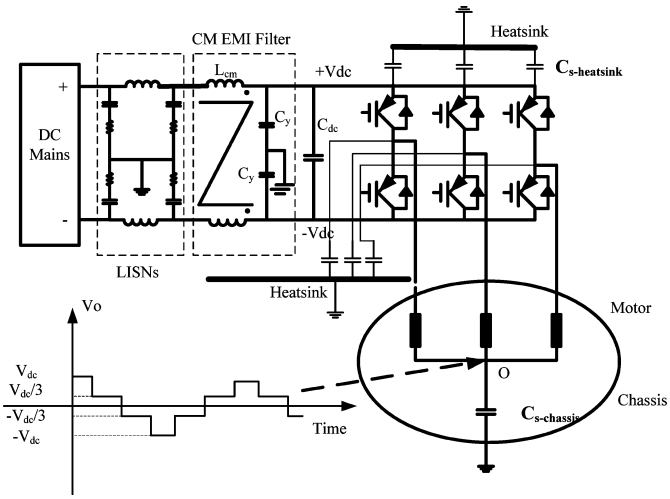

Fig. 1. Motor drive EMI test setup.

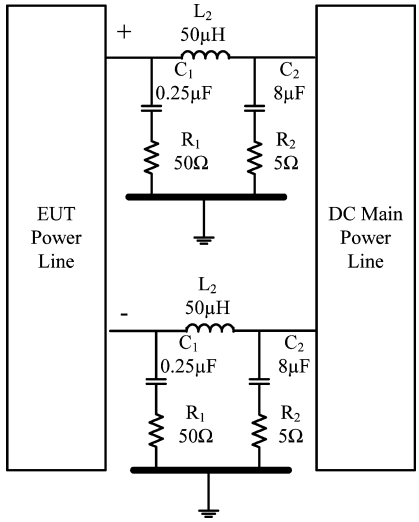

Fig. 2. LISN schematic from MIL-461 standard.

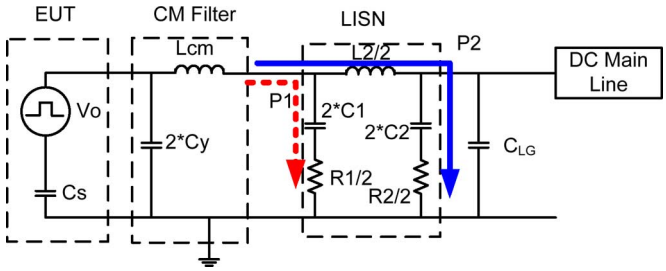

Fig. 3. Equivalent CM path for motor drive system.

These analyses also tell the differences between standard test and real application.

The paper first introduces the EMI test setup for a dc-fed three-phase motor drive system, and then, an analysis on CM EMI propagation path is given in Section II. Based on this analysis, a model to evaluate CM voltage and volt-second across the CM inductor is presented in Section III. Furthermore, an analysis is presented in this section on the issues that can impact CM voltage. Then, a new CM choke core selection criterion is introduced in Section VI. Simulation and experimental results are shown in the last part.

II. Analysis of CM EMI Path

An EMI test setup for a motor drive system with an LC CM filter is shown in Fig. 1. The EMI test setup is defined by MIL-STD-461E, which is a commonly used EMI standard for motor drive. It defines LISN parameters, ground connection, feeder length, load connection, etc., for different power ratings and applications. The EMI test setup exactly follows the standard. The motor drive power rating and the load are chosen according to the application needs. In Fig. 1, C_y is the CM capacitor (100 nF in this application); $C_{\text{s-heatsink}}$ is the stray capacitance between the power stage and ground (including cable CM stray capacitance), which is usually in the tens of picofarads; $C_{\text{s-chassis}}$ is the stray capacitance between the motor windings and chassis, which is several nanofarads in this case. For safety concerns, the motor chassis is grounded in practical applications. Point O is the equivalent ac midpoint of a three-phase load. The voltage of point O varies due to different switch combinations during the modulation, as shown in Fig. 1. Here, the LISN is defined by military standard MIL-STD-461E, and the EMI measurement frequency ranges from 10 kHz to 10 MHz. The schematic of the LISN is shown in Fig. 2. The motor drive is using center alignment for space-vector modulation in our analyses and experiment.

Here, equivalent parallel capacitance (EPC) of the CM choke is usually very small, and starts to impact the inductor impedance beyond several hundred kilohertzs. If it is designed carefully, the EPC can be even smaller so that it would not affect inductor impedance below several megahertzs. The fundamental frequency of CM voltage is at tens of kilohertzs, which is the same as switching frequency. Hence, within this frequency range, the impedance of EPC is much higher than that of the inductor. Because of this, the noise current will still go through the inductor path, so the EPC can be neglected in the equivalent circuit. Two C_y capacitances are symmetrical. They are X7R ceramic capacitors with a tolerance less than $\pm 10\%$. The small difference between these two capacitors will result in a small DM current because of the unbalanced grounding impedance [11]. However, these two capacitors are installed close to a huge dc-link capacitor, which provides a short circuit for high-frequency DM current. Hence, the small difference between these two CM capacitor does not significantly influence the equivalent circuit.

With all the assumptions above, the CM noise path shown in Fig. 1 can be simplified in a equivalent circuit shown in Fig. 3. In Fig. 3, $C_s = C_{\text{s-chassis}}$, and C_{LG} is the line-to-ground stray capacitance inside the dc main, which is usually very small. To conduct CM noise, two LISNs are in parallel. C_1 and C_2 are capacitors in LISN shown in Fig. 2.

Fig. 3 has two practical paths for CM current: P1 and P2. The calculated path impedances are shown in Fig. 4. The figure shows that the impedance of P2 is lower than P1 at frequencies below 150 kHz. The fundamental frequency of CM

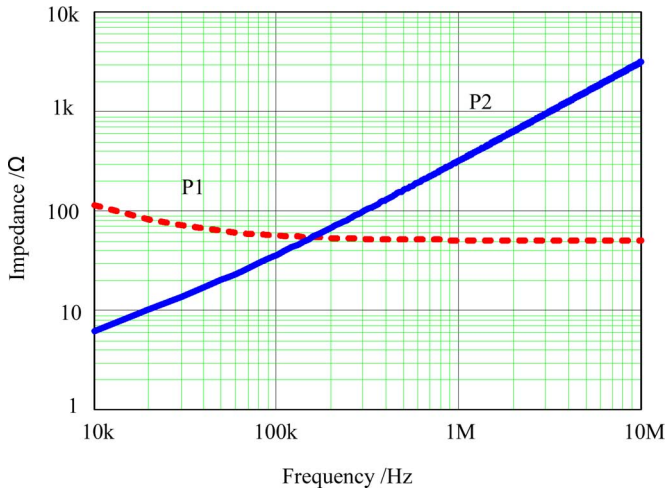

Fig. 4. Impedance of Paths 1 and 2.

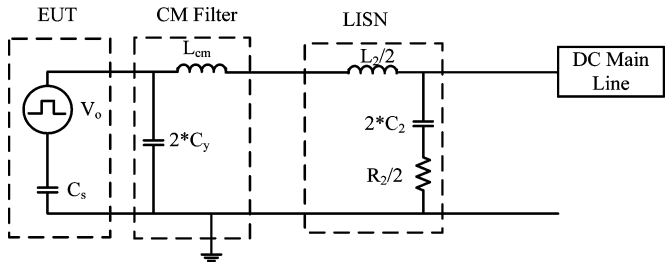

Fig. 5. Simplified CM path below 150 kHz.

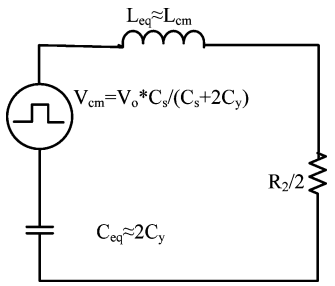

Fig. 6. Equivalent loop of CM path when frequency is lower than 150 kHz.

voltage $V_{\rm o}$ is equal to the switching frequency [7] at around 10 kHz, which is much lower than 150 kHz. Thus, the CM noise path can be further simplified into the schematic in Fig. 5. Furthermore, components $V_{\rm o}$, C_s, and C_y can be replaced by a Thevenin's equivalent circuit, as shown in Fig. 6. In real cases, because $2C_2 \gg 2C_y \gg C_s$, $C_{\rm eq} \approx C_y$. Similar to $C_{\rm eq}$, when $L_{\rm cm} \gg L_2$, $L_{\rm eq} \approx L_{\rm cm}$. For most motor drive applications, the switching frequency is below 150 kHz, and the CM voltage source frequency is the same as switching frequency, so the volt-second on the CM inductor is determined by the resonant circuit shown in Fig. 6.

According to the analysis in this section, the CM noise path in motor drive systems can be treated as an *RLC* circuit parallel with a CM voltage source. The CM voltage source characteristics (amplitude, shape, etc.) is determined by the three-phase output neutral point waveform and the ratio between stray capacitance and C_y capacitor. This CM voltage is divided by the R, L, C components in the equivalent circuit, the CM voltage drop on the inductor $L_{\rm CM}$, is a key factor that determines saturation of the CM choke.

Here, LISNs are necessary components in EMI noise test. LISN extracts noise signal from the power line, and this noise signal is measured and compared with the standard limits. However, in final application, there is no LISN sitting on the power line. It is just part of the EMI test. However, when doing the EMI test, LISNs create a low-impedance grounding path that increases the CM volt-second across the CM choke. LISN does not change the noise level, but does change the CM flux density inside choke. CM choke needs bigger volume/core to avoid saturation during the EMI test just to meet the standard, but in the real application, the volume of the CM choke can be smaller without the saturation flux density.

III. Saturation of CM Inductor Due to the CM Volt-Second

Based on the conclusions in Section II, CM voltage of the neutral point is a cause for CM choke saturation. Since the CM volt-second across the inductor can be considered as a voltage response in an *RLC* resonant circuit, which is proportional to the CM voltage source, there are two aspects that are related to the CM volt-second on the CM choke: CM path resonance and CM voltage source amplitude. Furthermore, CM voltage source characteristic is related to the converter modulation scheme. More details of how the CM voltage can influence the CM chokes are further discussed in this section.

A. Saturation of CM Inductor Due to the Resonance in CM EMI Path

Based on the analysis of the CM noise path, the CM voltage is applied to the CM inductor through the CM path. The CM noise propagation path in Fig. 6 is a typical *RLC* resonant circuit. When the system is designed with a selected modulation scheme, CM voltage pattern should be fixed, and if the motor drive is working at a constant operating point, the modulation index is fixed too. Hence, the CM voltage is constant and can be calculated according to the CM voltage pattern and vector length. The motor drive in our experiment is using conventional continuous SVM, center alignment, three-phase modulation. The corresponding CM voltage $V_{\rm o}$ waveform is shown in Fig. 7. The amplitude of equivalent CM voltage $V_{\rm cm}$ shown in Fig. 6 can be represented by (1), where the volt-second of the CM voltage has a direct impact on the magnetic flux density inside the CM inductor. Here, T_s is the time of the switching cycle and T_0 is the zero vector time. In Fig. 7, S_a, S_b, and S_c represent the switching function of each phase leg [15], and V_0, V_1, and V_2 stand for different vectors within this sector

$$|V_{\rm cm}| = \frac{(T_0|V_{\rm dc}| + (T_s - T_0)|(1/3)V_{\rm dc}|)}{T_s} \frac{C_s}{C_s + 2C_y}. \quad (1)$$

The volt-second on the CM inductor determines the CM flux density inside the CM magnetic core. The effects of the

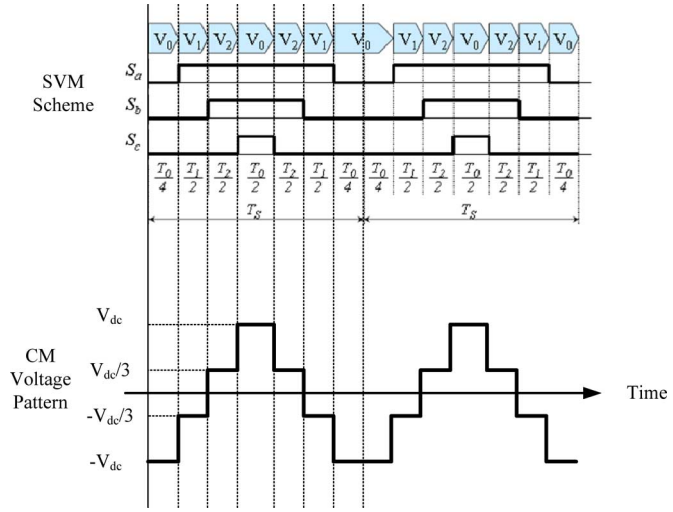

Fig. 7. CM voltage time-domain waveform.

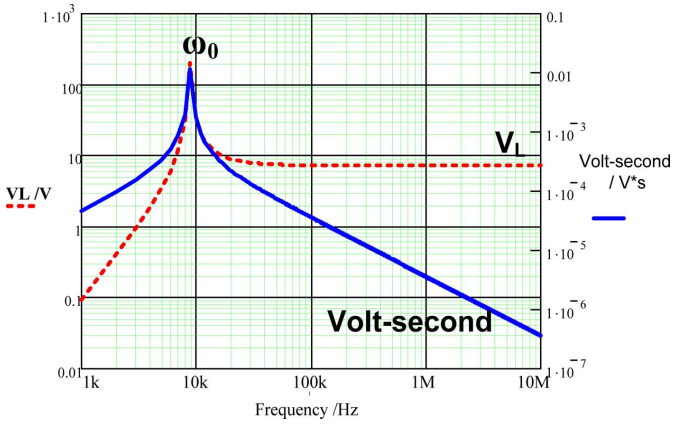

Fig. 8. Inductor voltage and volt-second versus frequency.

volt-second on the inductor can be represented by a sine wave, which has the same average value [as shown in (1)] within a half-cycle. The CM voltage on the CM inductor is given in (2). Here, the CM voltage is represented by a sine wave. The CM volt-second across the CM inductor is represented by (3)

$$|V_L| = \frac{\pi |V_{\rm cm}| \omega L_{\rm cm}}{2\sqrt{R_{\rm eq}^2 + \omega^2 L_{\rm cm}^2 \left(1 - (\omega_0^2/\omega^2)\right)^2}} \tag{2}$$

$$|\mathrm{VS}_L| = \int_0^{Ts/2} |V_L| \sin(\omega t) dt = \frac{\pi |V_{\rm cm}| L_{\rm cm}}{\sqrt{R_{\rm eq}^2 + \omega^2 L_{\rm cm}^2 (1 - (\omega_0^2/\omega^2))^2}}. \tag{3}$$

Here, $\omega_0 = 1/\sqrt{L_{\rm cm} C_{\rm eq}}$, and ω is the angular frequency of CM voltage source $V_{\rm cm}$.

According to (2) and (3), we can calculate the CM volt-second over the CM inductor, as shown in Fig. 8. Here, and in the following simulation, it is assumed that $L_{\rm cm} = 3$ mH and $C_s = 5$ nF. The curve in Fig. 8 shows that the CM volt-second is higher as the CM voltage frequency gets closer to the resonant frequency of the CM path loop; this is especially true for a high-Q network. Usually, in EMI filter design, adding small resistors can obviously damp the resonant peak. But too much resistance can also block the high-frequency noise path. The resistance here includes dc- and ac-related loss. Those are not negligible parts. Therefore, eventually, the circuit itself can provide a certain level of damping. If the leakage of the CM choke is designed to be within a given range, the CM flux inside the core dominates in core saturation. The CM inductor design should meet the condition in (4). The CM inductance value is determined by (5)

$$B_{\max} \geq \frac{V_L \times \Delta T}{N \times A_c} \tag{4}$$

$$L_{\rm cm} = \frac{\mu_0 \mu_r A_c N^2}{l_e}. \tag{5}$$

Here, N is the winding number of turns, A_c is the cross-section area of magnetic core, l_e is the length of the magnetic path, and $B_{\max}$ is the saturation flux density of the magnetic material.

In this paper, SVM modulation scheme is assumed to be conventional continuous, center alignment, three-phase modulation. The conclusion fits all three-phase commutation, center alignment, right/left alignment. These kinds of SVM modulations can reset the CM flux inside CM choke every switching cycle, because positive and negative volt-second are equal within one switching cycle at a fixed operating point. However, if other kinds of SVM modulation scheme are used, for example, 60°-clamped (see [15, DPWM1]), zero vector is unique (ppp or nnn) in a sector, so that the polarity of CM volt-second stays the same in a sector and flips over in the adjacent sector, the integral of the volt-second in two sectors will be zero. This will cause a dc bias inside the core in one sector and make the magnetic core bigger to avoid saturation. The CM flux inside core is reset every two sectors, that is one-third of the output line period. More detail on how modulation scheme influences the CM voltage are shown in [14], [15], and [20]. Each modulation scheme can be projected to a CM voltage pattern and the CM voltage and volt-second can be calculated.

B. Saturation of CM Inductor Due to Different Modulation Indexes

According to the analysis in Section II, the amplitude of CM voltage is another issue that impacts the CM magnetic component saturation. With a selected modulation scheme, the amplitude of the CM voltage is determined by the length of zero vectors, which is linked to the motor drive modulation index and operating point. The motor drive operating point is always changing according to the variation of input voltage/output current. This is directly related to different modulation indexes. Different modulation indexes lead to different zero vector lengths, which result in different CM voltage amplitudes. For example, when the motor drive is starting up, the modulation index is low to limit the starting current, so the CM voltage will be much higher; when the motor drive is running at the rated speed, the modulation index is higher, so the CM voltage is relatively lower. The variation of the CM voltage at different modulation

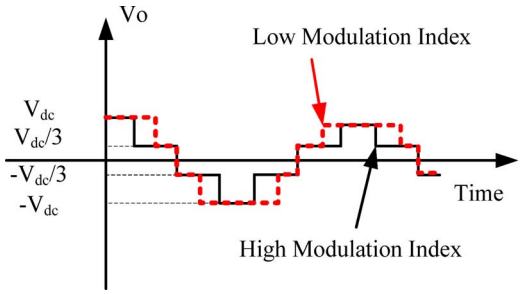

Fig. 9. Different CM voltages at different modulation index.

indexes is shown in Fig. 9. According to (1), lower modulation index corresponds to longer T_0, while a higher modulation index corresponds to shorter T_0. The modulation index changes the CM noise waveform and CM noise volt-second. For an extreme case, the CM volt-second when the modulation index is zero is twice as large as the volt-second when the modulation index is 1.

Understanding this can help determine how to design EMI filters for different conditions. Some EMI filters work well at the rated operating point, but do not work well for light load/low-speed operation due to the higher CM voltage.

IV. Design Guidelines for CM Inductors Based on CM Noise Constraint

In previous designs, the leakage inductance of CM inductor is used as DM inductance, and the DM current is considered as the main cause for CM choke saturation. The CM choke cross-section area is usually designed according to the leakage inductance value and DM current level. Then, a core that has enough window area to fit all the windings to achieve a certain CM inductance value is selected. The temperature rise is then verified. If the temperature rise is within limit, then the design is finished; otherwise, a bigger core is selected and the process is repeated. A design flowchart can be found in additional reference [12]. In addition to the previous design method, the CM volt-second is introduced to the core selection. The CM volt-second can be calculated incorporated with the converter design.

With the information of the CM voltage and CM noise path, the minimum volume of the CM magnetic component needed to avoid saturation can be estimated. From (3)–(5), the relationship of total magnetic volume to loop impedance (resonant frequency) and CM voltage frequency is derived and represented by (6). A visual representation is shown in Fig. 10. The following equation can be also used as a criterion in CM choke core selection:

$$A_c \times l_e \geq \frac{\pi \mu_0 \mu_r L_{cm} |V_{cm}|^2}{B_{max}^2 (R_{eq}^2 + \omega^2 L_{cm}^2 (1 - \omega_0^2/\omega^2)^2)} = \left(\frac{|VS_L|}{B_{max}}\right)^2 \frac{\mu_0 \mu_r}{L_{cm}}. \quad (6)$$

According to Fig. 10, when designing a CM choke for a high-power-density application, the design should avoid the resonant peaks to avoid high CM volt-second and high magnetic volume.

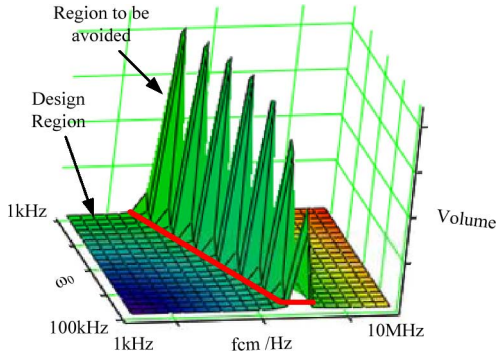

Fig. 10. Relationship among total magnetic volume and resonant.

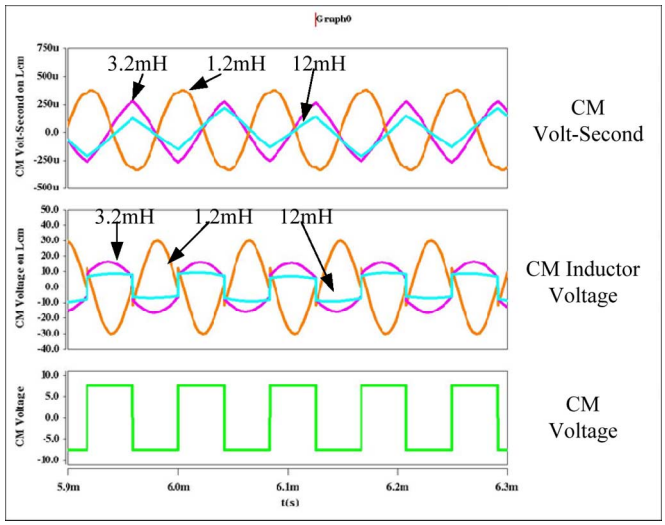

Fig. 11. CM voltage/volt-second on the CM inductor when CM inductor at different values.

Knowing the relationship between the modulation index and the CM volt-second, EMI filters should be designed to fit different operating conditions. When designing CM inductors, the lowest modulation index should be taken as the worst case for the CM volt-second constraint.

V. Simulation and Experiments

A Saber model is built based on Fig. 1. Fig. 11 shows the volt-second differences when L_{cm} is 1.2, 3, and 12 mH; C_y is 100 nF; and C_s is set to be 5 nF. According to the simulation, when L_{cm} varies from low to high, the resonant frequency of the CM path loop changes from 14 to 4.5 kHz. When $L_{cm} =$ 1.2 mH, the $\omega_0 = 14$ kHz, which is closer to the frequency of the CM voltage ($f_{cm} = 12$ kHz); when $L_{cm} = 3.2$ mH, $\omega_0 =$ 9 kHz, which is moving away from f_{cm}, and the CM voltage on the CM inductor is lower; when $L_{cm} = 12$ mH, where ω_0 is farther from f_{cm}, which gives the lowest CM volt-second on the CM choke.

An experiment is also established following Fig. 1, with a 2-kW motor drive, a 2-kW fan load, and two LISNs defined by MIL-STD-461. The drive is powered by a 300 Vdc source. The CM noise is extracted from the total noise using a noise

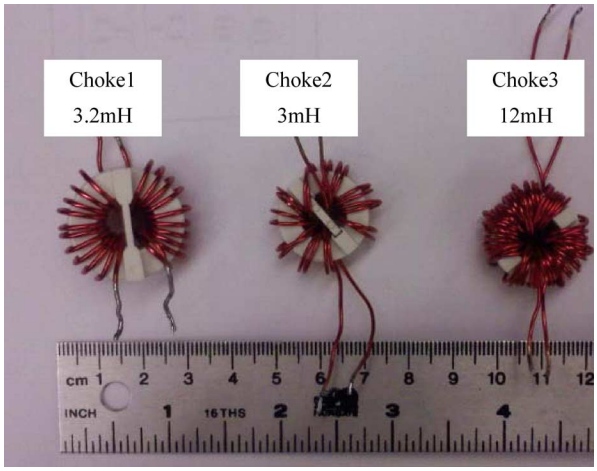

Fig. 12. CM Inductor using different core/different inductance.

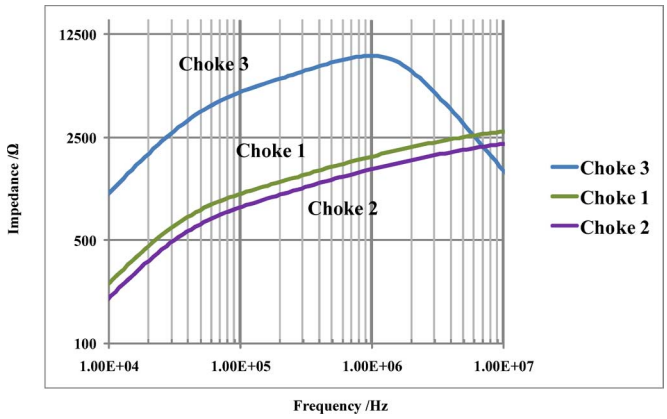

Fig. 13. Small-signal impedance measurement.

separator [8], [9]. An *LC* CM EMI filter is designed based on the CM bare noise, and the $2 \times C_y$ capacitor is 200 nF, as shown in Fig. 1. The CM choke core is a Finemet nanocrystalline core [8]. Three chokes are built, and are shown in Fig. 12. Choke 1 and choke 2 use different cores with the same inductance value (3 mH). Taking all windings into consideration, the choke size of choke 2 and choke 3 is 3799 mm^3, approximately half that of Choke 1(7359 mm^3). Choke 2 and Choke 3 use the same small cores. Choke 3 has twice the number of winding turns as choke 2. Thus, the inductance of choke 3 (12 mH) is four times greater than that of choke 2. Fig. 13 shows the small-signal impedance measurements of these three CM chokes using an Agilent 4294 A impedance analyzer. This is impedance of the CM inductance: two windings are in parallel and measured. The inductance values matches with the impedances measured, at least for low frequencies. For example, at the point of 30 kHz, impedance 12 mH choke is around 2262 Ω, the impedance of 3 mH is 565 Ω, and the impedance of 3.2 mH is 603 Ω, a bit higher than 3 mH.

The inductance varies as the frequency increases because the permeability of the material drops fast with increasing frequency. This is the characterization of the magnetic material, which explains why the impedances drop gradually with frequencies. At high frequencies, the EPC dominates the impedance, and then, the impedance drops down. Skin effect and proximity effect are also important high-frequency effects. They also increase the inductor high-frequency impedances. However, in our case here, they are not the key factors that determine the CM choke impedances compared to other factors.

The parameters of the cores are shown in Table I.

Fig. 14 shows the time-domain waveforms of the CM filter during the motor drive startup, as tested with choke 1. Since the motor drive is using vector modulation, at start up at low speed, the zero vectors are longer. This leads to a higher CM volt-second compared with the rated operating point. Thus, the CM choke is saturated at low speeds when the motor drive starts up, even if the DM current is very low. This is the phenomenon analyzed in Section IV. When the motor drive is running at the rated speed, the zero vector and the CM volt-second are reduced; the CM choke is then desaturated and resumes working. Fig. 15 shows the CM time-domain waveform tested with choke 2 (3 mH, small core) in two cases: with LISNs and without LISNs. The case with LISNs has been analyzed in Sections II and III, and has been shown to contain a low-impedance path to ground, so that it may saturate the CM inductor when f_{cm} is close to the resonant frequency. With LISNs, the CM voltage on the CM inductor is higher, so the CM inductor is saturated. When LISNs are removed, there is no low-impedance path between ground and the line side; furthermore, the line-to-ground capacitance of the dc main side is low (C_{LG}). This results in a very high loop resonant frequency that is far away from f_{cm}; as a result the CM voltage on the CM inductor is suppressed. In the experiment, the CM flux is measured with a CM transformer [9]. The principle of CM transformer is introduced in [9]. The two windings of the CM choke is the primary winding of the transformer. The secondary winding is the sensing winding. It has just one turn and terminates with a 1 MΩ resistor, and the CM voltage can be sensed across this resistor using oscilloscope. The input impedance of the oscilloscope channel is also set to be 1 MΩ. The output impedance of sensing winding should be as high as possible so that the sensing signal can precisely repeat the CM voltage across the CM inductor in the system. Meanwhile, since the output impedance is high, the current on the sensing resistor is very low so that the CM transformer will not disturb the motor drive operation. In this way, CM voltage time-domain waveform can be measured in oscilloscope.

The frequency-domain measurement is achieved with LISN and spectrum analyzer. Noise signals are extracted from LISNs and connected to noise separator [11] through coaxial cable. The CM noise is combined and extracted from the line noise signals, and is input into the spectrum analyzer.

The CM voltage in Figs. 14 and 15 are measured on the C_y capacitors. When the core is saturated, the switching combination and vector length are still the same, but the saturated inductor will have resonance with the C_y capacitor, which makes the CM voltage higher. Here, the CM voltage on the C_y capacitors is the same as the voltage across the inductor since the loop resistance is small.

Fig. 16 shows a comparison of the DM and CM current with two different chokes in the time-domain waveform. Choke 1

TABLE I
FINEMET CORE PARAMETERS USED IN THE EXPERIMENTS

	Core Part Number	Ac(mm^2)	le(mm)	Volume(mm^3)	Number of Turns
Choke 1	F1AH0695	22.2	56.5	4876	11*2
Choke 2	F1AH0654	11.3	47.1	2596	12*2
Choke 3	F1AH0654	11.3	47.1	2596	28*2

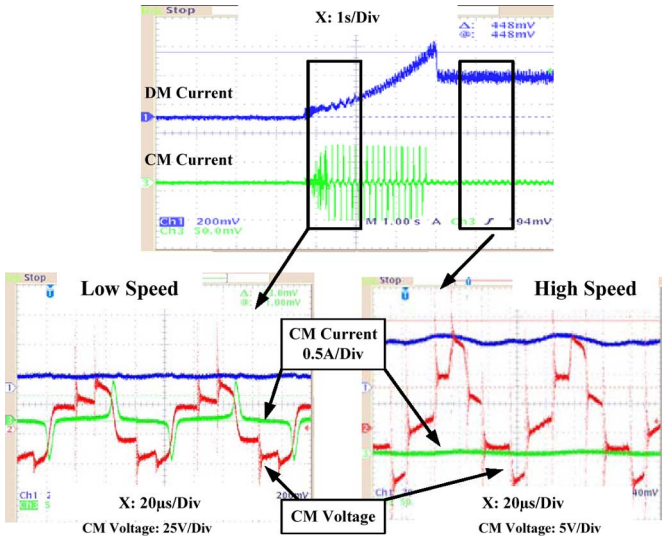

Fig. 14. Time-domain waveforms of CM filter performance during motor drive startup.

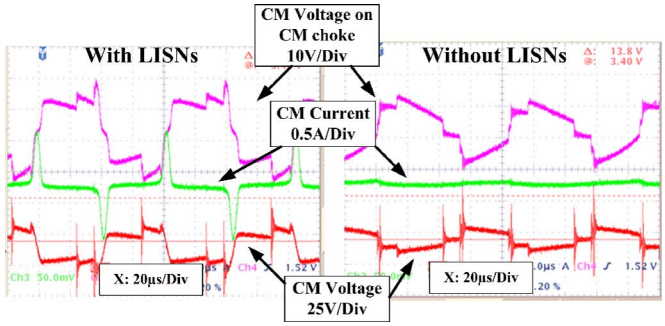

Fig. 15. Time-domain waveforms with and without LISNs.

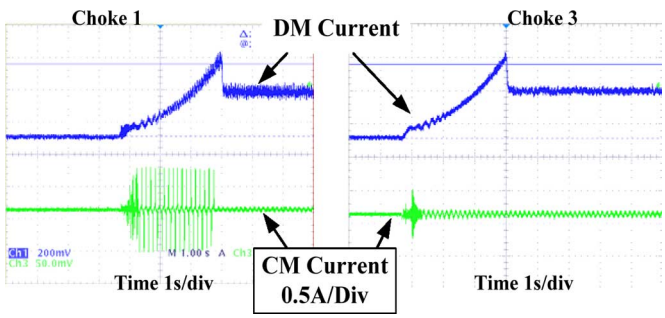

Fig. 16. Time-domain waveform of different chokes at motor drive startup.

(3.2 mH) with a big core has a longer saturation time during the startup, which means choke 1 does not work at low speed. Choke 3 (12 mH) is not saturated during startup and is capable of operating at low speed.

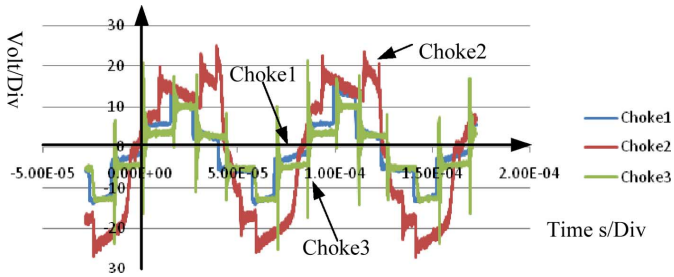

Fig. 17. CM inductor voltage comparison of different chokes using CM transformer.

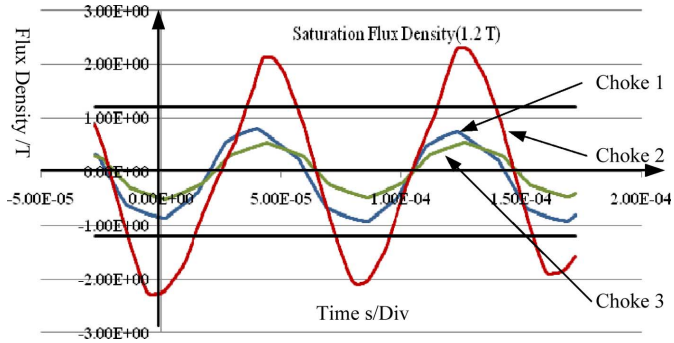

Fig. 18. Time-domain waveform of flux density inside core.

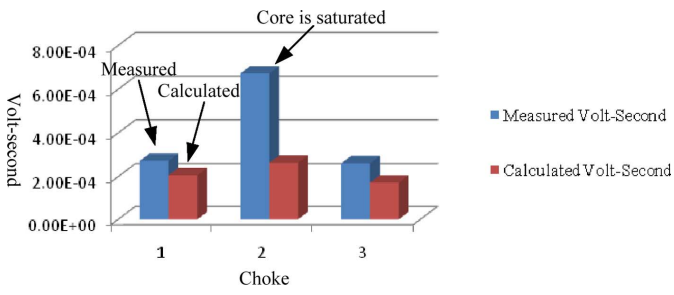

Fig. 19. Comparisons of calculated and measured volt-second.

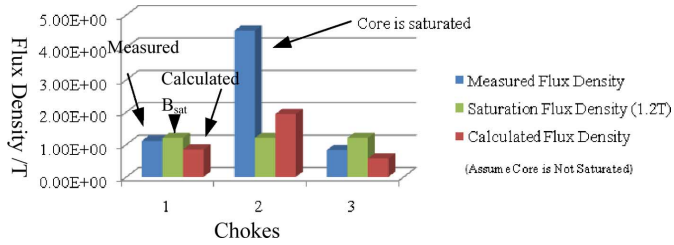

Fig. 20. Comparisons of calculated and measured flux density.

TABLE II
COMPARISON OF $A_c \times l_e$ PRODUCT

		Ac*le(m^3)	Cal_result (3.2mH) (m^3)	Cal_result (12mH) (m^3)
Choke 1	F1AH0695	$1.254*10^{-6}$	$1.46*10^{-6}$	$3.89*10^{-7}$
Choke 2 and Choke 3	F1AH0654	$5.32*10^{-7}$	$1.59*10^{-6}$	$4.25*10^{-7}$

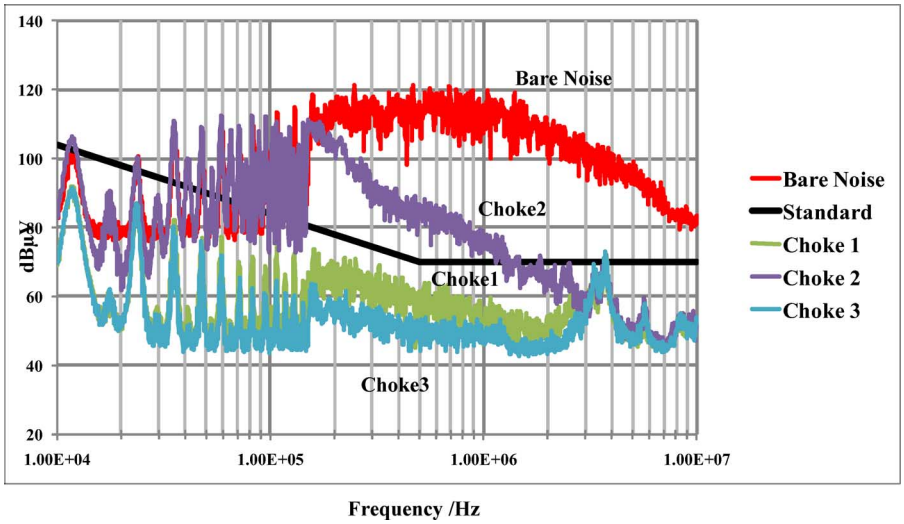

Fig. 21. In-circuit noise measurement.

Fig. 17 shows the measured CM inductor time-domain voltage waveform when using the CM transformer. The flux density inside the core can be calculated based on the CM inductor volt-second measurement. According to Fig. 17, the CM voltage can be approximated like Fig. 7, where $T_s = 83\ \mu$s and $T_0 = 22.3\ \mu$s. The equivalent CM voltage amplitude can be represented by (1). The CM volt-second across the CM inductor can be calculated using (1)–(3). The flux density can be extracted by numerical integration of the waveforms in Fig. 17. Fig. 18 shows the flux density time-domain waveforms based on the measurement in Fig. 17. According to the waveforms, choke 2 is saturated. The saturation flux density limits are also shown in the figure. Theoretically, choke 2 has almost the same volt-second as choke 1, but choke 2 has fewer turns and a much smaller cross-section area, which makes the $B_{\max}$ in choke 2 higher.

In Fig. 17, the voltage across the CM inductor is higher when the CM choke is saturated. This phenomenon can be explained using the equivalent circuit in Fig. 6. The current going through the CM path is equal to the current going through the CM choke, with charges $C_{\rm eq}$ in a CM voltage half-cycle. The voltage across the CM inductor is equal to the sum of $\rm Vc_{eq}$, $V_{\rm cm}$, and $V_{\rm Req}$. When the CM choke is saturated in one of the CM voltage half cycles, the voltage of $C_{\rm eq}$ increases as a result of the increase in the inductor current. In the following half-cycle, the voltages $\rm Vc_{eq}$ and $V_{\rm cm}$ are positively added, which causes the CM choke voltage to increase.

The result of Fig. 18 is not directly measured on the oscilloscope. It is obtained based on the data recorded from Fig. 17. A total of 2000 data points are recorded in two switching cycles of CM voltage across the CM inductor, as shown in Fig. 17, and the volt-second can be simply obtained by doing numerical integration. Knowing the volt-second, number of turns, and the cross-section area of the CM choke, flux density can be calculated, as shown in Fig. 18.

The calculated volt-second and measured volt-second are shown in Fig. 19. The flux density can also be calculated and measured, as shown in Fig. 20.

Table II shows the comparisons of calculated result using (6) and the product of $A_c \times l_e$ in the real core. The product of $A_c \times l_e$ is the product of the cross section and the magnetic length from the datasheet; and Cal_result (3.2 mH) is the calculated $A_c \times l_e$ product using (6) when $L_{\rm cm}$ is 3.2 mH. This result shows the required minimum $A_c \times l_e$ when $L_{\rm cm}$ is 3.2 mH. Similarly, Cal_result (12 mH) is the calculated $A_c \times l_e$ product using (6) when $L_{\rm cm}$ is 12 mH. The equivalent permeability of these two cores (F1AH0654 and F1AH0695) has slight differences according to the real measurement in the datasheet, which results in two different calculated $A_c \times l_e$ products. According to these results, when $L_{\rm cm} = 3.2$ mH, the minimum required $A_c \times l_e$ is 1.59×10^{-6} m^3, which is larger than the $A_c \times l_e$ of the smaller core F1AH0654, and the big-core F1AH0695 can avoid saturation. When $L_{\rm cm}$ is increased to 12 mH, the minimum required $A_c \times l_e$ is around 4.25×10^{-7} m^3, which is smaller than the product of $A_c \times l_e$ in the F1AH0654 core, so we can choose the smaller core F1AH0654 instead of the big-core F1AH0695 for the CM inductor.

Fig. 21 shows the CM noise measurement with different CM chokes. Although choke 1 and choke 2 have approximately the same small-signal impedance, their in-circuit performances are totally different, because choke 2 is saturated with a smaller core. The in-circuit test also shows that even with a smaller core, choke 3 can still perform well with the increased $L_{\rm cm}$ by avoiding the resonant frequency in the CM path loop close to $f_{\rm cm}$. Applying (6), with a given converter, if the CM voltage $V_{\rm o}$

is known, we can determine the minimum volume for the CM magnetic core.

At high frequencies beyond 1 MHz, the permeability of cores drops to a very low value, which is even closer to the permeability of air. Therefore, in the end, at high frequencies, the impedance of chokes merge, as shown in Fig. 13, causing the EMI spectrums to merge as in Fig. 21. Furthermore, there are many issues other than the CM chokes that impact high-frequency attenuation. Wang *et al*. [22] proved that the grounding impedance and the coupling between two ground connections impact the filter high-frequency attenuation. Coupling between passive components is proved to be another important issue in [11], [21], and [22] that determines the high-frequency attenuation. These reasons can also cause the EMI noise to merge at high frequencies.

VI. Conclusion

In this paper, a new mechanism with two aspects for CM inductor saturation and its impacts on the CM magnetic component volume are analyzed. The CM noise path resonance plays an important role here. It can cause the CM noise voltage to resonate in the loop, and makes the CM volt-second over the CM inductor high enough to saturate the CM inductor. The CM voltage source is related to the modulation index and dc-bus voltage such that the lower the modulation index is, the higher the CM voltage volt-second will be. The LISNs in the CM loop create a low grounding impedance path that brings the CM noise path to the resonant frequency. This is closer to the CM voltage frequency f_{cm}, which makes the CM inductor suffer from a higher CM volt-second and results in a higher CM inductor volume. The experiments carried out verify the analysis. A new criterion is proposed for high power density CM chokes design based on above knowledge.

References

[1] H. Chen, Z. Qian, S. Yang, and C. Wolf, "Finite-element modeling of saturation effect excited by differential-mode current in a common-mode choke," *IEEE Trans. Power Electron.*, vol. 24, no. 3, pp. 873–877, Mar. 2009.

[2] R. Anne, B. Hans, D. Zhao, B. Ferreira, and L. Frank, "A new behavioral model for performance evaluation of common mode chokes," in *Proc. 2007 Int. Zurich Symp. Electromagn. Compat.*, pp. 501–504.

[3] H. Hemphill and B. Wallertz, "Critical core parameters in the design of common mode suppression chokes," in *Proc. 1995 Int. Zurich Symp. Electromagn. Compat.*, pp. 334–336.

[4] Y. Sun, A. Esmaeli, L. Sun, and E. Kang, "Investigation and suppression of conducted EMI and shaft voltage in induction motor drive system," in *Proc. 2006 World Congr. Intell. Control Autom.*, pp. 8256–8259.

[5] A. Esmaeli, B. Jiang, and L. Sun, "Modeling and suppression of PWM inverter's adverse effects," in *Proc. 2006 Int. Symp. Syst. Control Aerosp. Astronautics*, pp. 1450–1454.

[6] A. Esmaeli, K. Zhao, L. Sun, and Q. Wu, "Investigation and suppression of the adverse effects of PWM inverter through passive filter technique," in *Proc. IEEE 2006 Conf. Ind. Electron. Appl.*, pp. 1–4.

[7] G. L. Skibinski, R. J. Kerkman, and D. Schlegel, "EMI emissions of modern PWM AC drives," *IEEE Ind. Appl. Mag.*, vol. 5, no. 6, pp. 47–80, Nov. 1999.

[8] (2009). [Online]. Available: http://metglas.com/downloads/finemet/FMCMC190804.pdf

[9] C. Khun, W. Khan-ngern, and M. Kando, "Passive EMI filter performance improvements with common mode voltage cancellation technique for PWM inverter," in *Proc. IEEE 2007 Int. Conf. Power Electron. Drive Syst.*, pp. 257–261.

[10] S. Wang, Y. Maillet, F. Wang, R. Lai, R. Burgos, and F. Luo, "Investigating the grounding of EMI filters in power electronics systems," in *Proc. IEEE 2008 Power Electron. Spec. Conf.*, pp. 1625–1631.

[11] S. Wang, "Characterization and cancellation of high-frequency parasitics for EMI filters and noise separators in power electronics applications," Ph.D. dissertation, Dept. Electr. Eng., Virginia Polytech. Inst. State Univ., Blacksburg, VA, 2005.

[12] Y. Y. Maillet, "High-density discrete passive EMI filter design for Dc-Fed motor drives," Master's Thesis, Dept. Electr. Eng., Virginia Polytech. Inst. State Univ., Blacksburg, VA, 2008.

[13] D. Zhao, J. A. Ferreira, A. Roc'h, and F. Leferink, "Common-mode DC-bus filter design for variable-speed drive system via transfer ratio measurements," *IEEE Trans. Power Electron.*, vol. 24, no. 2, pp. 518–524, Feb. 2009.

[14] T. P. Chen, "Common-mode ripple current estimator for parallel three-phase inverters," *IEEE Trans. Power Electron.*, vol. 24, no. 5, pp. 1330–1339, May 2009.

[15] A. M. Hava and E. Un, "Performance analysis of reduced common-mode voltage PWM methods and comparison with standard PWM methods for three-phase voltage-source inverters," *IEEE Trans. Power Electron.*, vol. 24, no. 1, pp. 241–252, Jan. 2009.

[16] L. Ran, S. Gokani, J. Clare, K. J. Bradley, and C. Christopoulos, "Conducted electromagnetic emissions in induction motor drive systems. II. Frequency domain models," *IEEE Trans. Power Electron.*, vol. 13, no. 4, pp. 768–776, Jul. 1998.

[17] H. Akagi and T. Oe, "A specific filter for eliminating high-frequency leakage current from the grounded heat sink in a motor drive with an active front end," *IEEE Trans. Power Electron.*, vol. 23, no. 2, pp. 763–770, Mar. 2008.

[18] H. Akagi and T. Shimizu, "Attenuation of conducted EMI emissions from an inverter-driven motor," *IEEE Trans. Power Electron.*, vol. 23, no. 1, pp. 282–290, Jan. 2008.

[19] M. R. Baiju, K. K. Mohapatra, R. S. Kanchan, and K. Gopakumar, "A dual two-level inverter scheme with common mode voltage elimination for an induction motor drive," *IEEE Trans. Power Electron.*, vol. 19, no. 3, pp. 794–805, May 2004.

[20] A. M. Hava, N. O Cetin, and E. Un, "On the contribution of PWM methods to the common mode (leakage) current in conventional three-phase two-level inverters as applied to AC motor drives," in *Proc. IEEE Ind. Appl. Soc. Annu. Meeting*, 2008, pp. 1–8.

[21] S. Wang, F. C. Lee, D. Y. Chen, and W. G. Odendaal, "Effects of parasitic parameters on EMI filter performance," *IEEE Trans. Power Electron.*, vol. 19, no. 3, pp. 869–877, May 2004.

[22] S. Wang, Y. Y. Maillet, F. Wang, R. Lai, R. Burgos, and F. Luo, "Investigating the grounding of EMI filters in power electronics systems," in *Proc. IEEE Power Electron. Spec. Conf.*, 2008, pp. 1625–1631.

Fang Luo (S'06) received the Bachelor's degree from Huazhong University of Science and Technology, Wuhan, China, in 2003 and the Ph.D. degree from Huazhong University of Science and Technology, Hubei, China, in 2010.

Since 2007, he has been with the Center for Power Electronics Systems (CPES), Virginia tech, Blacksburg, as a Visiting Student, supported by the Chinese Scholarship Council and CPES. His experience in power electronics includes research and development on uninterrupted power supply (UPS) systems, battery monitoring and management system, and dc power distribution network protection. His current research interests include high-density electromagnetic interference (EMI) filtering solution and passive EMI filter integration in motor drive systems.

Shuo Wang (S'03–M'06–SM'07) received the B.S.E.E. degree from Southwest Jiaotong University, Chengdu, China, in 1994, the M.S.E.E. degree from Zhejiang University, Hangzhou, China, in 1997, and the Ph.D. degree from the Center for Power Electronics Systems (CPES), Virginia Polytechnic Institute and State University (Virginia Tech), Blacksburg, in 2005.

Since 2009, he has been with Electrical Power Systems, GE Aviation Systems, Vandalia, OH. From 2005 to 2009, he was a Research Assistant Professor at the Center for Power Electronics Systems, Virginia Tech. He holds four U.S. patents and has another two pending. He has authored or coauthored more than 70 academic papers in the IEEE Transactions and IEEE conferences. His current research interests include EMI/EMC in power electronics systems, high-density power conversion, three-phase power conversion and inversion, motor drive, generator control, and power systems.

Dr. Wang received the 2005 Best Transaction Paper Award from the IEEE TRANSACTIONS ON POWER ELECTRONICS and the William M. Portnoy Award for the best paper published in the IEEE IAS Annual Conference in 2004. He is an Associate Editor for the IEEE TRANSACTIONS ON INDUSTRY APPLICATIONS.

Fei (Fred) Wang (S'85–M'91–SM'99–F'10) received the B.S. degree from Xi'an Jiaotong University, Xi'an, China, and the M.S. and Ph.D. degrees from the University of Southern California, Los Angeles, in 1982, 1985, and 1990, respectively, all in electrical engineering.

From 1990 to 1992, he was a Research Scientist in the Electric Power Laboratory, University of Southern California. In 1992, he joined the GE Power Systems Engineering Department, Schenectady, NY, as an Application Engineer. From 1994 to 2000, he was a Senior Product Development Engineer with GE Industrial Systems, Salem, VA. During 2000 to 2001, he was the Manager of Electronic and Photonic Systems Technology Laboratory, GE Global Research Center, Schenectady, and Shanghai, China. In 2001, he joined the Center for Power Electronics Systems (CPES), Virginia Polytechnic Institute and State University (Virginia Tech), Blacksburg, as a Research Associate Professor and became an Associate Professor in 2004. During 2003, he was the CPES Technical Director. Since 2009, he has been with the University of Tennessee and Oak Ridge National Laboratory, Knoxville, TN, as a Professor and the Condra Chair of Excellence in power electronics. His current research interests include power electronics, power systems, controls, electric machines, and motor drives.

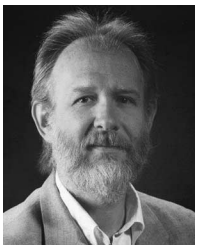

Dushan Boroyevich (S'81–M'86–SM'03–F'06) received the Dipl.Ing. degree from the University of Belgrade, Belgrade, Serbia, in 1976, the M.S. degree from the University of Novi Sad, Novi Sad, Serbia, in 1982, and the Ph.D. degree from Virginia Polytechnic Institute and State University (Virginia Tech), Blacksburg, in 1986.

From 1986 to 1990, he was an Assistant Professor and the Director of the Power and Industrial Electronics Research Program in the Institute for Power and Electronic Engineering, University of Novi Sad, and later, the Acting Head of the institute. He then joined the Bradley Department of Electrical and Computer Engineering, Virginia Tech, as an Associate Professor, where he is currently the American Electric Power Professor in the department and the Codirector of the Center for Power Electronics Systems (CPES). His current research interests include multiphase power conversion, electronic power distribution systems, power electronics systems modeling and control, and multidisciplinary design optimization.

Dr. Boroyevich is a recipient of the IEEE William E. Newell Power Electronics Technical Field Award.

Nicolas Gazel was born in Paris, France. He received the Master's degree in electrical engineering from the École Speciale de Mécanique et d'Electricité, France, in 2001.

Since 2001, he has been a Design Engineer with Safran Group, Hispano-Suiza, Moissy Cramayel, France. He has been associated with CPES, Virginia Tech, since 2007. He was engaged in power electronics, which includes research and development project leading on electromagnetic interference (EMI) and power-quality items for ac and dc-fed three-phase motor drive application, and lightning strike indirect effect in composite environment for aircraft. His current research interests include high-density EMI filtering solution and passive EMI filter integration in motor drive systems.

Yong Kang was born in Hubei Province, China, on October 16, 1965. He received the B.E., M.E., and Ph.D. degrees from Huazhong University of Science and Technology, Wuhan, China, in 1988, 1991, and 1994, respectively.

In 1994, he joined Huazhong University of Science and Technology as a Lecturer and was promoted to Associate Professor in 1996 and to a Full Professor in 1998. He is currently the Head of the College of Electrical and Electronic Engineering, Huazhong University of Science and Technology. He is the author or coauthor of more than 60 technical papers. His current research interests include power electronic converter, ac drivers, electromagnetic compatibility, and their digital control techniques.

Andrew Carson Baisden (S'03) received the B.S. degree in electrical engineering from Illinois Institute of Technology, Chicago, in 2003, the second B.S. degree in mathematics from Benedictine University, Lisle, IL, in 2003, and the M.S. degree in electrical engineering and the Ph.D. degree from Center for Power Electronics Systems (CPES), Virginia Tech, Blacksburg, VA, in 2006 and 2009, respectively.

During 2000–2002, he was a Research Lab Assistant as a Summer Intern at Argonne National Laboratories. In the summer of 2006, he was a Power Electronics Development Engineer for Rockwell Automation. From 2003 to 2009, he was with the CPES as a Graduate Research Assistant. He is currently at Johns Hopkins University Applied Physics Laboratory, Laurel, MD, as a Power Electronics Engineer for space applications. His research interests include electromagnetic interference, electronics packaging, power converter systems, and integrated power-electronic systems.